Dyadic Point Spread Functions for 3D Inverse Source Imaging Based on Analytical Integral Solutions

Georg Schnattinger[*] and Thomas F. Eibert

Abstract—Imaging is a valuable tool for solving inverse source problems. The achievable image quality is determined by the imaging system. Its performance can be evaluated by using the concept of point spread functions (PSFs). It is common to compute the PSFs using a numerical algorithm. However, in some cases the PSFs can be derived analytically. In this work, new analytical PSFs are presented. The results apply to scalar and dyadic scenarios in 3D originating from acoustics and electromagnetics. Data sets with narrow angular acquisition or complete spherical coverage are considered, where broadband and narrowband frequency domain data is supported. Several visualizations accompany the resulting formulas. Finally, the analytical PSFs are verified using a numerical implementation of the imaging process.

1. INTRODUCTION

Imaging is a well-known methodology which proved to be useful in many fields ranging from medical to military applications. Since imaging problems can be computationally intensive, several fast algorithms have been developed: Fourier-based techniques [1], hierarchical algorithms [2–4] and the backprojection method [5] to name a few. The resulting images are influenced by many parameters such as frequency, bandwidth and angular scan range. These influences can be characterized by employing the concept of point spread functions (PSF). In [6], for example, the author presents scalar 2D PSFs for various data acquisition parameters. In [7], scalar 3D PSFs are computed for several circular aperture configurations. PSFs for specific scenarios in passive radar and medical imaging are presented in [8, 9]. In [10, 11], analytical solutions are derived for a projection electron system and a Doppler radar. To characterize the imaging procedure for solving a full vectorial inverse problem using the concept of PSFs, it is necessary to define the PSFs in a dyadic fashion, cf. [12, 13]. In this work, scalar and dyadic PSFs will be derived analytically for elementary acquisition geometries in the k-space domain. To the best knowledge of the authors, the results presented in this work have not been published before with minor exceptions [12–15], which are clearly indicated in the text.

Section 2 introduces two different imaging scenarios to identify the mathematical expressions for the derivation of the PSF. The first expression leads to a scalar PSF whereas the second expression results in a dyadic PSF. Analytical results for both cases are derived in Section 3. To validate the analytical results, numerical computations have been carried out in Section 4. Finally, some conclusions are drawn in Section 5.

2. INVERSE SOURCE SCENARIOS

In this section, both a scalar and a dyadic PSF will be defined in two steps. First, two linear inverse source problems will be introduced and then, imaging concepts are employed to solve them. In this way, the resulting images correspond to a convolution between PSF and source distribution.

* Corresponding author: Georg Schnattinger (georg.schnattinger@tum.de).
The authors are with the Lehrstuhl für Hochfrequenztechnik, Technische Universität Müchen, Munich 80290, Germany.

2.1. Acoustic or Scalar Imaging

A scalar inverse source problem is for example encountered in optoacoustics [16], where acoustic waves are caused by the absorption of optical energy. Acoustic pressure waves are solutions of the scalar wave equation [16]

$$\left(\Delta - \frac{1}{c^2}\frac{\partial^2}{\partial t^2}\right)\rho(\mathbf{r},t) = \frac{\partial}{\partial t}h(\mathbf{r},t), \tag{1}$$

where ρ is the pressure depending on the position $\mathbf{r}$ and the time t, c is the propagation velocity in the background medium and h is the amount of energy absorbed per unit volume and per unit time. Since the optical propagation velocity by far exceeds the acoustic propgation velocity, it is valid to set $h(\mathbf{r}) = q(\mathbf{r})\delta(t)$. Transforming (1) to the frequency domain utilizing this substitution yields

$$\left(\Delta + k^2\right)\rho(\mathbf{r},\omega) = j\omega q(\mathbf{r}), \tag{2}$$

where $k = \omega/c$ is the wavenumber and ω is the angular frequency. By employing the concept of Green's functions [17, S. 851], the solution to this time-harmonic differential equation can be written as

$$\rho(\mathbf{r},\omega) = -\frac{j\omega}{4\pi}\iiint\limits_{V'} q\left(\mathbf{r}'\right)\frac{e^{-jk\|\mathbf{r}-\mathbf{r}'\|_2^2}}{\|\mathbf{r}-\mathbf{r}'\|_2^2}d^3\mathbf{r}'. \tag{3}$$

This function describes the linear relationship between the source and its radiated pressure waves. An image of the source distribution shall be generated based on observations surrounding the source. The conventional way of imaging is a 3D Fourier transform in the k-space domain reading as

$$\hat{q}(\mathbf{r}) = \iiint\limits_{K}\rho_{\text{FF}}(\mathbf{k})e^{-j\mathbf{k}\cdot\mathbf{r}}d^3\mathbf{k} = \mathscr{F}\{M_K(\mathbf{k})\rho_{\text{FF}}(\mathbf{k})\}, \tag{4}$$

where

$$\rho_{\text{FF}}(\mathbf{k}) = -\frac{4\pi}{jck}\lim_{r'\to\infty}\frac{r'}{e^{-jkr'}}\rho\left(r'\hat{k},ck\right) = \iiint\limits_{V'}q(\mathbf{r}')e^{j\mathbf{k}\cdot\mathbf{r}'}d^3\mathbf{r}'. \tag{5}$$

is referred to as the normalized far-field spectrum of the source.

Depending on the amount of data available, the generated image might look differently. This is incorporated by the integration volume K, which corresponds to the locations of the observations in the k-space domain. The masking function M_K represents this information loss within the Fourier transform denoted by the letter $\mathscr{F}$.

Inserting (5) into (4) and changing the order of the volume integrals results in

$$\hat{q}\left(\mathbf{r}\right) = \iiint\limits_{V'}\iiint\limits_{K}e^{-j\mathbf{k}\cdot(\mathbf{r}-\mathbf{r}')}d^3\mathbf{k}q\left(\mathbf{r}'\right)d^3\mathbf{r}' = P(\mathbf{r})*q(\mathbf{r}). \tag{6}$$

Thus, the image corresponds to a convolution between the PSF

$$P(\mathbf{r}) = \iiint\limits_{K}e^{-j\mathbf{k}\cdot\mathbf{r}}d^3\mathbf{k} = \mathscr{F}\{M_K(\mathbf{k})\} \tag{7}$$

and the source distribution q.

2.2. Full Vectorial Imaging

In the second scenario, this formulation is extended to a full vectorial inverse source problem. The source is a vectorial frequency invariant electric current distribution and the observations are performed using the radiated electric field [12, 13]. In this case, the radiation is described by the curl-curl equation of the electric field which reads as [18, S. 465]

$$\nabla \times \nabla \times \mathbf{E}(\mathbf{r},\omega) - k^2\mathbf{E}(\mathbf{r},\omega) = -j\omega\mu\mathbf{J}(\mathbf{r}), \tag{8}$$

where $\mathbf{E}$ is the electric field, μ is the magnetic permeability and $\mathbf{J}$ is the electric current density. By employing the same concepts as in the scalar case, it is possible to derive the normalized plane wave spectrum

$$\mathbf{E}_{\mathrm{FF}}(\mathbf{k}) = \left(\bar{\mathbf{I}} - \hat{k}\hat{k}\right) \cdot \iiint\limits_{V'} \mathbf{J}\left(\mathbf{r}'\right) e^{j\mathbf{k}\cdot\mathbf{r}'} d^3\mathbf{r}'. \tag{9}$$

As can be seen from (5), it differs, because it features the additional factor $\bar{\mathbf{I}} - \hat{k}\hat{k}$ and it is based on a vectorial integral. When computed by a vectorial Fourier transform, the image

$$\hat{\mathbf{J}}(\mathbf{r}) = \mathscr{F}\{M_K(\mathbf{k})\mathbf{E}_{\mathrm{FF}}(\mathbf{k})\} \tag{10}$$

corresponds to the minimum energy solution according to [13] and therefore represents the radiating currents of the source. Analogously to (6), the expression is reformulated as a convolution. Thus, the image depends on the source distribution through

$$\hat{\mathbf{J}}(\mathbf{r}) = \bar{\mathbf{P}}(\mathbf{r}) \overset{\circ}{*} \mathbf{J}(\mathbf{r}), \tag{11}$$

where $\overset{\circ}{*}$ denotes a scalar product where the resulting multiplicative expressions are replaced by convolutions. The associated dyadic PSF reads as

$$\bar{\mathbf{P}}(\mathbf{r}) = \mathscr{F}\left\{M_K(k)\left(\bar{\mathbf{I}} - \hat{k}\hat{k}\right)\right\} = P(\mathbf{r})\bar{\mathbf{I}} - \mathscr{F}\left\{M_K(k)\hat{k}\hat{k}\right\}, \tag{12}$$

where $P(\mathbf{r})$ refers to the corresponding scalar PSF in (7).

3. POINT SPREAD FUNCTION

An important property of the Fourier transform is its rotational invariance [19, pp. 28]. Applying this principle to the scalar PSF in (7) results in

$$P(\mathbf{R}\mathbf{r}) = \mathscr{F}\{M(\mathbf{R}\mathbf{k})\}, \tag{13}$$

where $\mathbf{R} \in \mathbb{R}^{3\times3}$ is a rotation matrix. So, a rotation in the k-space domain implies a similar rotation in the spatial domain. Thus, performing the Fourier transform for any rotated version of a specific masking function $M(\mathbf{k})$ is sufficient to calculate the PSF. In case of the dyadic PSF from (12), the rotational invariance principle reads as

$$\bar{\mathbf{P}}(\mathbf{R}\mathbf{r}) = \mathscr{F}\left\{M(\mathbf{R}\mathbf{k})\left(\bar{\mathbf{I}} - \mathbf{R}\hat{k}\mathbf{R}\hat{k}\right)\right\}. \tag{14}$$

Therefore, the dyadic reference coordinate system must also be rotated appropriately.

3.1. Narrow Angle Narrow Bandwidth Approximation

In many scenarios, measurement data is only acquired in a small angular sector and with small relative bandwidth, i.e., consider radar measurements of an airborne target from a ground platform. This effect of filling only a small portion of the k-space with data will be modeled by the masking function

$$M(\mathbf{k}) = \begin{cases} 1, & \mathbf{k} \in K \\ 0, & \mathbf{k} \notin K \end{cases}, \tag{15}$$

where the k-space domain K is defined as

$$\mathbf{k} = k \begin{pmatrix} \cos\phi\sin\theta \\ \sin\phi\sin\theta \\ \cos\theta \end{pmatrix} \in K \Longleftrightarrow \begin{matrix} 2|\phi - \phi_0| \le \Delta\phi \\ 2|\theta - \theta_0| \le \Delta\theta \\ 2|k - k_0| \le \Delta k \end{matrix}. \tag{16}$$

Since the k-space data is limited to a narrow angle narrow bandwidth volume, the variables $\Delta\phi$, $\Delta\theta$ and Δk are assumed to be small. Due to the rotational invariance principle in (13), the aspect angles ϕ_0, θ_0 and the center wavenumber k_0 can be chosen arbitrarily. In [12], results are derived for $\theta_0 = \pi/2$ and $\phi_0 = 0$. This choice is adopted in the following and implies that the line of sight is aligned with the x-axis.

3.1.1. Scalar

The spherical integral resulting from (7) and (15) reads as

$$\int_{-\frac{\Delta k}{2}}^{\frac{\Delta k}{2}} \int_{-\frac{\Delta \phi}{2}}^{\frac{\Delta \phi}{2}} \int_{-\frac{\Delta \theta}{2}}^{\frac{\Delta \theta}{2}} e^{-j\mathbf{k}\cdot\mathbf{r}}\mathbf{k}\cdot\mathbf{k}\sin\theta d\theta d\phi dk. \tag{17}$$

By approximating both the prefactor of the exponential and its exponent using a multivariate Taylor series of absolute order one around ϕ_0, θ_0 and k_0, the integral can be solved analytically and results in

$$P(\mathbf{r}) = \mathscr{F}\{M(\mathbf{k})\} = k_0^2 \Delta\phi\Delta\theta\Delta k e^{-jk_0 x} g_1(\Delta\mathbf{k},\mathbf{r},k_0), \tag{18}$$

where

$$g_1(\Delta\mathbf{k},\mathbf{r},k_0) = \operatorname{si}\left(\frac{\Delta\phi k_0 y}{2}\right)\operatorname{si}\left(\frac{\Delta\theta k_0 z}{2}\right)\left[\left(1-\frac{j2}{k_0 x}\right)\operatorname{si}\left(\frac{\Delta k x}{2}\right)+\frac{j2}{k_0 x}\cos\left(\frac{\Delta k x}{2}\right)\right] \tag{19}$$

with

$$\operatorname{si}(x) = \frac{\sin x}{x}. \tag{20}$$

As it turns out, the resolution is determined by the width of the si-function. Therefore, the resolution in x-direction mostly depends on the bandwidth Δk. In contrast to this, the resolution in y and z-direction only depends on the center frequency through k_0 and not on the bandwidth. In order to visualize the PSF, a scenario has been created which consists of three isotropic point sources located at

$$\frac{\mathbf{r}_1}{\lambda_{\min}} = \begin{pmatrix} 2.4 \\ 2.7 \\ 0 \end{pmatrix}, \quad \frac{\mathbf{r}_2}{\lambda_{\min}} = \begin{pmatrix} -2.7 \\ -2.7 \\ 2.4 \end{pmatrix}, \quad \frac{\mathbf{r}_3}{\lambda_{\min}} = \begin{pmatrix} 0 \\ 0 \\ -2.4 \end{pmatrix}. \tag{21}$$

Figure 1 has been computed by convolving the point spread function in (18) with these point scatterers. The 3D complex-valued images are visualized by projecting the maximum amplitudes onto the faces of a cube. The resolution with respect to each of the Cartesian coordinates is determined by $\Delta\phi = \frac{\pi}{3}$, $\Delta\theta = \frac{\pi}{4}$, $k = 2\pi$ and $\Delta k = 2\pi$.
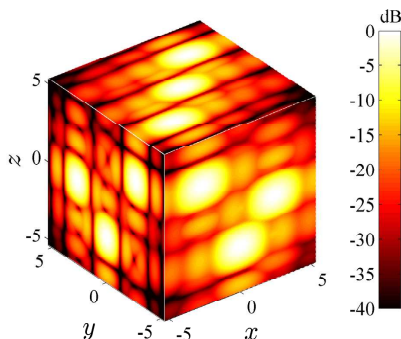

Figure 1. Image of scatterers in (21) for the k-space acquisition geometry in (16) generated using (18) for $\Delta\phi = \frac{\pi}{3}$, $\Delta\theta = \frac{\pi}{4}$, $\lambda_{\max} = 2\,\mathrm{m}$ and $\lambda_{\min} = 1\,\mathrm{m}$ while x, y and z are measured in wavelengths ($\lambda_{\min}$).

As already mentioned, the solution in (18) is based on a first order Taylor expansion of the prefactor and the exponent of the integrand in (17). More accurate approximations of the integral can be derived using higher order Taylor expansions. This leads to more complicated integrals and unfortunately their solution is tedious. However, computer algebra systems can be of assistance. In this work, MuPAD [20], which is distributed as a MATLAB [21] toolbox, was employed. A multivariate Taylor expansion is performed by specifying the absolute order n and weighting coefficients w_k, w_ϕ, w_θ. A higher weight reduces the order of the expansion with respect to the selected variable. In Table 1, a collection of parameter sets is presented for which MuPAD can solve the approximated integral in (17) analytically. The parameter set in the second row matches the assumptions for (18). All solutions

Table 1. Heuristic complexity estimation (evaluated with MuPAD) of analytical solution of integral in (17) approximated by expansion of prefactor and exponent in integrand utilizing multivariate Taylor series expansion with absolute order n and weighting cofficients w_k, w_f, w_θ.

Prefactor		Exponent		Absolute Scalar
n	$[w_k, w_\phi, w_\theta]$	n	$[w_k, w_\phi, w_\theta]$	Heuristic Complexity
1	[2, 1, 1]	1	[1, 1, 1]	46
1	[1, 1, 1]	1	[1, 1, 1]	87
1	[1, 1, 1]	2	[2, 1, 1]	258
2	[1, 1, 1]	1	[1, 1, 1]	468
3	[1, 1, 1]	1	[1, 1, 1]	706
4	[1, 1, 1]	1	[1, 1, 1]	2232
2	[1, 1, 1]	2	[2, 1, 1]	2370
3	[1, 1, 1]	2	[2, 1, 1]	4623

below this row are of increasing complexity and therefore are not printed here. Instead, the table shows a quantitative measure for the heuristic complexity which was computed with the MuPAD command *length*. Additionally, the unhandy expressions can be used for simulations by employing automatic code generation. In the cases where the Taylor expansion of the exponent reaches an absolute order of $n = 2$, the solutions also rely on the error function

$$\text{erf}(x) = \frac{2}{\sqrt{\pi}} \int_0^x e^{-t^2} dt \tag{22}$$

and its extension to the complete complex plane. Thus, an efficient implementation of this function is required by the generated program code.

3.1.2. Dyadic

By applying similar techniques as in the scalar case to the dyadic integral

$$\int_{-\frac{\Delta k}{2}}^{\frac{\Delta k}{2}} \int_{-\frac{\Delta \phi}{2}}^{\frac{\Delta \phi}{2}} \int_{-\frac{\Delta \theta}{2}}^{\frac{\Delta \theta}{2}} e^{-j\mathbf{k}\cdot\mathbf{r}} \left(\mathbf{k} \cdot \mathbf{k}\bar{\mathbf{I}} - \mathbf{k}\mathbf{k}\right) \sin\theta d\theta d\phi dk \tag{23}$$

resulting from (12) and (15), the solution can be written as

$$\bar{\mathbf{P}}(\mathbf{r}) = k_0^2 \Delta\phi\Delta\theta\Delta k e^{-jk_0x} \begin{pmatrix} 0 & g_2(\Delta\mathbf{k}, \mathbf{r}, k_0) & g_3(\Delta\mathbf{k}, \mathbf{r}, k_0) \\ g_2(\Delta\mathbf{k}, \mathbf{r}, k_0) & g_1(\Delta\mathbf{k}, \mathbf{r}, k_0) & 0 \\ g_3(\Delta\mathbf{k}, \mathbf{r}, k_0) & 0 & g_1(\Delta\mathbf{k}, \mathbf{r}, k_0) \end{pmatrix}, \tag{24}$$

where $g_1(\Delta\mathbf{k}, \mathbf{r}, k_0)$ is given in (19) and

$$g_2(\Delta\mathbf{k}, \mathbf{r}, k_0) = \frac{j}{k_0 y} \text{si}\left(\frac{\Delta k x}{2}\right) \text{si}\left(\frac{\Delta\theta k_0 z}{2}\right) \left[\text{si}\left(\frac{\Delta\phi k_0 y}{2}\right) - \cos\left(\frac{\Delta\phi k_0 y}{2}\right)\right], \tag{25}$$

$$g_3(\Delta\mathbf{k}, \mathbf{r}, k_0) = \frac{j}{k_0 z} \text{si}\left(\frac{\Delta k x}{2}\right) \text{si}\left(\frac{\Delta\phi k_0 y}{2}\right) \left[\text{si}\left(\frac{\Delta\theta k_0 z}{2}\right) - \cos\left(\frac{\Delta\theta k_0 z}{2}\right)\right]. \tag{26}$$

As expected, Eq. (24) depends on the scalar PSF. In fact, the resulting image is quite similar to the dyadic PSF, but there are some interactions between the different vectorial components. In order to be able to compute an image from the sources in (21), the orientation of the currents must be defined. This is done by assigning

$$\mathbf{j}_1 = I_0 \mathbf{e}_x, \quad \mathbf{j}_2 = I_0 \mathbf{e}_y, \quad \mathbf{j}_3 = I_0 \mathbf{e}_z, \tag{27}$$

where I_0 is a unit current density.

Figure 2 was computed by convolving the dyadic PSF with these point sources using (11). Note that the $\mathbf{e}_x$-oriented current cannot be recognized properly, because it is perpendicular to the measurement aperture. Additionally, the dyadic formulation introduces polarization errors which limit the dynamic range of the imaging process.

Similar to the scalar case, the accuracy of the narrow angle narrow bandwidth approximation can be increased by employing higher order Taylor expansions. Feasible solutions of dyadic integral approximations and their heuristic complexities are presented in Table 2 for the same parameter sets
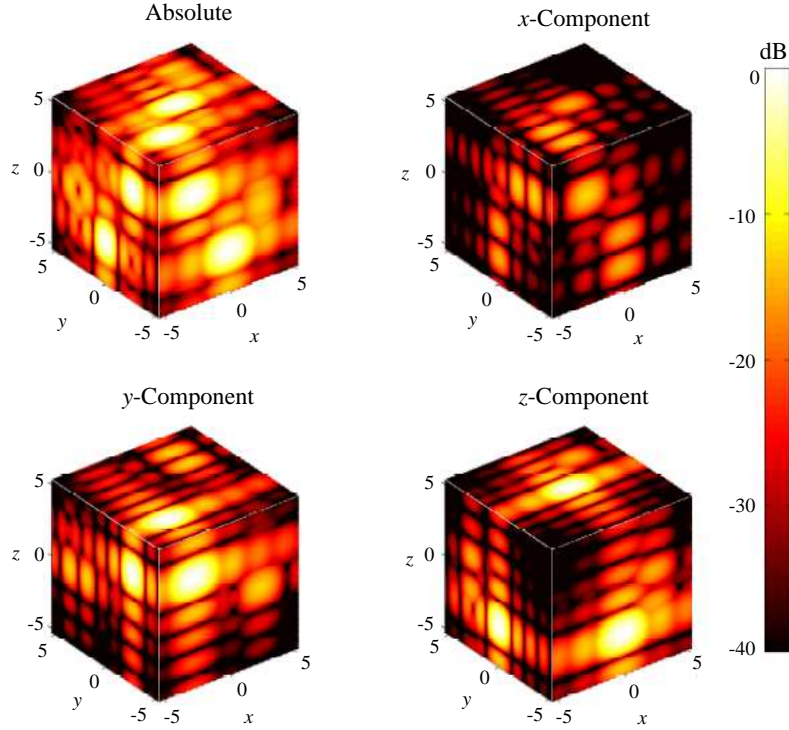
Figure 2. Image of currents positioned as in (21) and oriented as in (27) for the k-space acquisition geometry in (16) generated using (24) for $\Delta\phi = \frac{\pi}{3}$, $\Delta\theta = \frac{\pi}{4}$, $\lambda_{\max} = 2\,\mathrm{m}$ and $\lambda_{\min} = 1\,\mathrm{m}$ while x, y and z are measured in wavelengths ($\lambda_{\min}$).

Table 2. Heuristic complexity estimation (evaluated with MuPAD) of analytical solution of integral in (23) approximated by expansion of prefactor and exponent in integrand utilizing multivariate Taylor series expansion with absolute order n and weighting cofficients w_k, w_f, w_θ.

Prefactor		Exponent		Heuristic Complexity	
n	$[w_k, w_\phi, w_\theta]$	n	$[w_k, w_\phi, w_\theta]$	Abs. Dyadic	Rel. to Scalar
1	$[2, 1, 1]$	1	$[1, 1, 1]$	375	8.10
1	$[1, 1, 1]$	1	$[1, 1, 1]$	457	5.25
1	$[1, 1, 1]$	2	$[2, 1, 1]$	2165	8.39
2	$[1, 1, 1]$	1	$[1, 1, 1]$	2234	4.77
3	$[1, 1, 1]$	1	$[1, 1, 1]$	14860	21.1
2	$[1, 1, 1]$	2	$[2, 1, 1]$	16548	6.98
4	$[1, 1, 1]$	1	$[1, 1, 1]$	56160	25.2
3	$[1, 1, 1]$	2	$[2, 1, 1]$	69688	20.9

as in Table 1. In addition, the ratio between the heuristic complexities of the dyadic and the scalar solutions is computed. A growth factor of about 9 is roughly expected, because the dyad has nine entries and all of them are integrated. The parameter sets in the bottom rows of the table lead to solutions which grow faster than their scalar versions. Two parameter sets represent special solutions. The first row in the table corresponds to the solution in [12]. The second row exactly matches the assumptions for (24). Furthermore, the approximation errors induced by the solutions in rows 2, 3 and 8 for a specific test scenario are compared in Section 4.

3.2. Narrow Angle Finite Bandwidth Approximation

Since broadband imaging systems are getting more and more popular, it is desirable to have a PSF which is valid for large relative bandwidths. This can be modeled by replacing the constraint on k in (16) by

$$k_{\min} \leq k \leq k_{\max}. \tag{28}$$

In this case, a first order Taylor expansion of the integrand in (17) and (23) is only carried out with respect to the angles ϕ and θ but not for the wavenumber as in the last subsection.

3.2.1. Scalar

Solving (7) while using the narrow angle assumption leads to

$$P(\mathbf{r}) = \left[\frac{k}{yz} F_{E(\bullet)}(\Delta\phi y, \Delta\theta z, k, \mathbf{r}) \right]_{k_{\min}}^{k_{\max}} \tag{29}$$

where

$$
\begin{aligned}
F_{E(\bullet)}(a, b, k, \mathbf{r}) &= -E\left(j\frac{k}{2}(-2x + a + b) \right) - E\left(j\frac{k}{2}(-2x - a - b) \right) \\
&\quad + E\left(j\frac{k}{2}(-2x + a - b) \right) + E\left(j\frac{k}{2}(-2x - a + b) \right)
\end{aligned} \tag{30}
$$

with E denoting the exponential function

$$\mathrm{E}(x) = \frac{e^x}{x}. \tag{31}$$

Applying this PSF to the point sources in (21) yields the plot in Fig. 3. When comparing this plot to Fig. 1, where the narrow bandwidth approximation in (18) was applied for the same parameters, the approximation error becomes obvious. Note that better results can be obtained with the narrow bandwidth approximation by dividing the k-space data into narrow frequency bands and then superimposing the images obtained with the narrow bandwidth PSF.
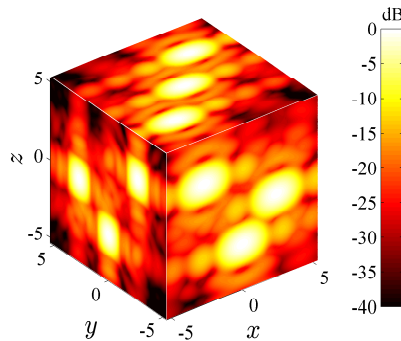

Figure 3. Image of scatterers in (21) for the k-space acquisition geometry in (16) altered by (28) generated using (29) for $\Delta\phi = \frac{\pi}{3}$, $\Delta\theta = \frac{\pi}{4}$, $\lambda_{\max} = 2\,\mathrm{m}$ and $\lambda_{\min} = 1\,\mathrm{m}$ while x, y and z are measured in wavelengths ($\lambda_{\min}$).

3.2.2. Dyadic

Solving the dyadic integral in (12) while using the narrow angle assumption yields

$$\bar{\mathbf{P}}(\mathbf{r}) = \begin{pmatrix} 0 & P_2(\mathbf{r}) & P_3(\mathbf{r}) \\ P_2(\mathbf{r}) & P(\mathbf{r}) & 0 \\ P_3(\mathbf{r}) & 0 & P(\mathbf{r}) \end{pmatrix}, \tag{32}$$

where $P(\mathbf{r})$ is the scalar PSF in (29) and

$$P_2(\mathbf{r}) = \left[\frac{\Delta\phi k}{2yz} G_{\mathrm{E}(\bullet)}(\Delta\phi y, \Delta\theta z, k, \mathbf{r}) + \frac{j}{y^2 z} F_{\mathrm{Ei}(\bullet)}(\Delta\phi y, \Delta\theta z, k, \mathbf{r}) \right]_{k_{\min}}^{k_{\max}}, \tag{33}$$

$$P_3(\mathbf{r}) = \left[\frac{\Delta\theta k}{2yz} G_{\mathrm{E}(\bullet)}(\Delta\theta z, \Delta\phi y, k, \mathbf{r}) + \frac{j}{yz^2} F_{\mathrm{Ei}(\bullet)}(\Delta\theta z, \Delta\phi y, k, \mathbf{r}) \right]_{k_{\min}}^{k_{\max}}. \tag{34}$$

The expression $F_{\mathrm{Ei}(\bullet)}$ refers to the definition in (30) with E being replaced by the exponential integral function

$$\mathrm{Ei}(x) = \int_{-\infty}^{x} \frac{e^t}{t} dt \tag{35}$$

and the expression $G_{\mathrm{E}(\bullet)}$ corresponds to

$$G_{\mathrm{E}(\bullet)}(a, b, k, \mathbf{r}) = -\mathrm{E}\left(j\frac{k}{2}(-2x + a + b) \right) + \mathrm{E}\left(j\frac{k}{2}(-2x - a - b) \right)$$
$$+ \mathrm{E}\left(j\frac{k}{2}(-2x + a - b) \right) - \mathrm{E}\left(j\frac{k}{2}(-2x - a + b) \right) \tag{36}$$

in conjunction with the exponential function in (31). The dyadic PSF is not a closed-form expression, because it depends on the exponential integral function in (35). Still, the expression can be evaluated conveniently using mathematics software. In MATLAB, a function with a very similar definition is called *expint*. Fig. 4 shows the resulting 3D images for the vectorial components using the scenario in (21) oriented as in (27).

3.3. Full Scan Range Zero Bandwidth Approximation

In some applications, the imaging systems only acquire data for a single frequency or for a limited number of frequencies. In this case, a proper image is only obtained when a wide angular scan range is used. In this section, it is assumed that measurement data is available for the complete sphere and therefore, the masking function is chosen as

$$M(\mathbf{k}) = w(k) \propto \delta(k - k_0) \tag{37}$$

and normalized according to

$$\iiint_K w(k) d^3\mathbf{k} = 1 \implies w(k) = \frac{\delta(k - k_0)}{k^2}. \tag{38}$$

3.3.1. Scalar

The PSF is derived by solving (7) while using (37). The familiar result which is also given in [13] reads as

$$P(\mathbf{r}) = \mathscr{F}\{w(k)\} = 4\pi\mathrm{si}(k_0 r). \tag{39}$$

Figure 5 shows an image generated with this PSF while the wavelength equals $\lambda = 1\,\mathrm{m}$. The image depicts the three point sources in (21). The points are clearly visible in the image, but the dynamic range of the image is poor.

Absolute   x-Component
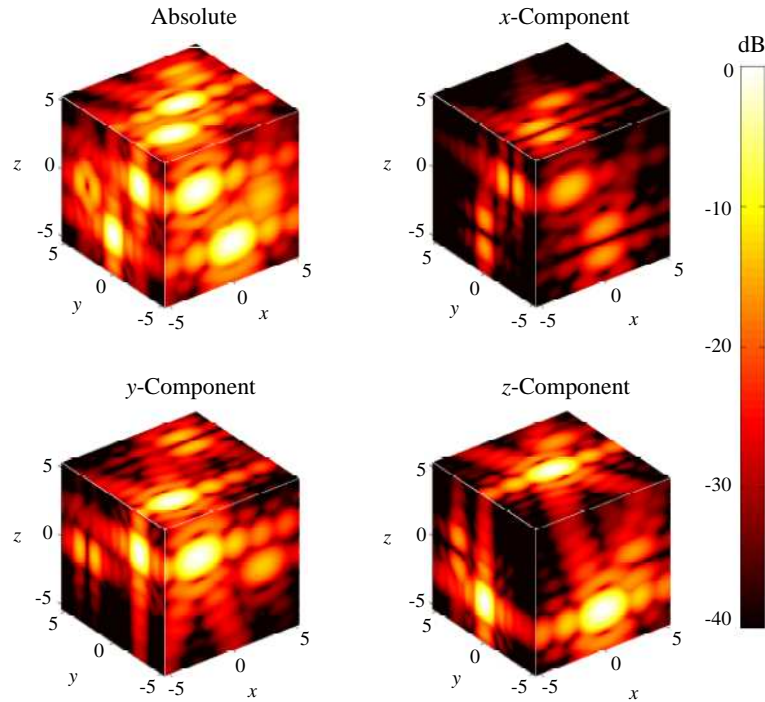
y-Component   z-Component

Figure 4. Image of currents positioned as in (21) and oriented as in (27) for the k-space acquisition geometry in (16) generated using (32) for $\Delta\phi = \frac{\pi}{3}$, $\Delta\theta = \frac{\pi}{4}$, $\lambda_{\max} = 2$ m and $\lambda_{\min} = 1$ m while x, y and z are measured in wavelengths ($\lambda_{\min}$).
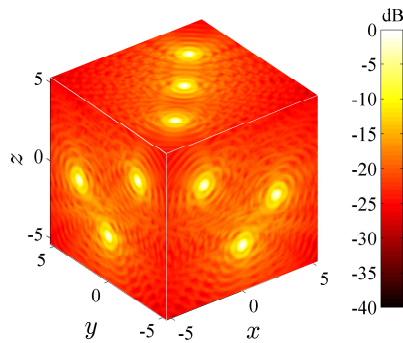
Figure 5. Image of scatterers in (21) for a monofrequent spherical k-space acquisition geometry generated using (39) for $\lambda = 1$ m while x, y and z are measured in wavelengths (λ).

3.3.2. Dyadic

For the derivation of the PSF, the second term of the dyadic integral in (12) using (37) is solved first. The expression can be split into two parts by

$$\mathscr{F}\left\{w(k)\hat{k}\hat{k}\right\} = \mathscr{F}\{w(k)\} * \mathscr{F}\left\{\hat{k}\hat{k}\right\}. \tag{40}$$

Prior to the evaluation of the Fourier expression $\mathscr{F}\{\hat{k}\hat{k}\}$, its symmetry will be analyzed. First of all, the vectors $\mathbf{r}$ and $\mathbf{k}$ are defined in spherical coordinates:

$$\mathbf{r} = r \begin{bmatrix} \cos\Phi\sin\Theta \\ \sin\Phi\sin\Theta \\ \cos\Theta \end{bmatrix}, \qquad \mathbf{k} = k \begin{bmatrix} \cos\phi\sin\theta \\ \sin\phi\sin\theta \\ \cos\theta \end{bmatrix}. \tag{41}$$

Then, the dyadic expression $\mathscr{F}\{\hat{k}\hat{k}\}$ is rewritten in a matrix representation utilizing spherical vector components:

$$\mathbf{q}(\mathbf{r}) = \mathscr{F}\left\{\left[\hat{k}\hat{k}\right]_{\hat{\Theta},\hat{\Phi},\hat{r}}\right\} = \mathscr{F}\left\{\begin{bmatrix} \hat{\Theta}\cdot\hat{k}\hat{k}\cdot\hat{\Theta} & \hat{\Theta}\cdot\hat{k}\hat{k}\cdot\hat{\Phi} & \hat{\Theta}\cdot\hat{k}\hat{k}\cdot\hat{r} \\ \hat{\Phi}\cdot\hat{k}\hat{k}\cdot\hat{\Theta} & \hat{\Phi}\cdot\hat{k}\hat{k}\cdot\hat{\Phi} & \hat{\Phi}\cdot\hat{k}\hat{k}\cdot\hat{r} \\ \hat{r}\cdot\hat{k}\hat{k}\cdot\hat{\Theta} & \hat{r}\cdot\hat{k}\hat{k}\cdot\hat{\Phi} & \hat{r}\cdot\hat{k}\hat{k}\cdot\hat{r} \end{bmatrix}\right\}. \tag{42}$$

Due to the rotational invariance of the Fourier transform, it is possible to perform the following substitutions:

$$\mathbf{r} = \mathbf{R}\mathbf{r}', \quad \mathbf{k} = \mathbf{R}\mathbf{k}', \tag{43}$$

$$\hat{\Theta} = \mathbf{R}\hat{\Theta}', \quad \hat{\theta} = \mathbf{R}\hat{\theta}', \tag{44}$$

$$\hat{\Phi} = \mathbf{R}\hat{\Phi}', \quad \hat{\phi} = \mathbf{R}\hat{\phi}', \tag{45}$$

$$\hat{r} = \mathbf{R}\hat{r}', \quad \hat{k} = \mathbf{R}\hat{k}'. \tag{46}$$

By simplifying the resulting expression, it can be shown that[†]

$$\mathbf{q}(\mathbf{R}\mathbf{r}') = \mathbf{q}(\mathbf{r}') \implies \mathbf{q}(\mathbf{r}) = \mathbf{q}(r\mathbf{e}_z). \tag{47}$$

Thus, the evaluation of the Fourier transform $\mathscr{F}\{\hat{k}\hat{k}\}$ for all $\mathbf{r}$ in the whole spatial domain can be reduced to an evaluation of the Fourier transform on the line segment $r\mathbf{e}_z$ combined with an evaluation of the spherical unit vectors in the whole spatial domain:

$$\mathscr{F}\left\{\hat{k}\hat{k}\right\} = \begin{bmatrix} \hat{\Theta} \\ \hat{\Phi} \\ \hat{r} \end{bmatrix}^T \mathscr{F}\left\{\left[\hat{k}\hat{k}\right]_{\mathbf{e}_x,\mathbf{e}_y,\mathbf{e}_z}\right\}\bigg|_{r\mathbf{e}_z} \begin{bmatrix} \hat{\Theta} \\ \hat{\Phi} \\ \hat{r} \end{bmatrix}. \tag{48}$$

The dyad $\hat{k}\hat{k}$ in Cartesian components reads as

$$\left[\hat{k}\hat{k}\right]_{\mathbf{e}_x,\mathbf{e}_y,\mathbf{e}_z} = \begin{bmatrix} \cos^2\phi\sin^2\theta & \cos\phi\sin\phi\sin^2\theta & \cos\phi\sin\theta\cos\theta \\ \cos\phi\sin\phi\sin^2\theta & \sin^2\phi\sin^2\theta & \sin\phi\sin\theta\cos\theta \\ \cos\phi\sin\theta\cos\theta & \sin\phi\sin\theta\cos\theta & \cos^2\theta \end{bmatrix}. \tag{49}$$

With these results, the analytical result of the Fourier transform in (40) can be derived as

$$\mathscr{F}\left\{w(k)\left[\hat{k}\hat{k}\right]_{\mathbf{e}_x,\mathbf{e}_y,\mathbf{e}_z}\right\}\bigg|_{\mathbf{r}=r\mathbf{e}_z}$$

$$= \frac{4\pi}{(k_0 r)^3}\left[(\sin(k_0 r) - k_0 r\cos(k_0 r))(\mathbf{e}_x\mathbf{e}_x + \mathbf{e}_y\mathbf{e}_y) + ((k_0^2 r^2 - 2)\sin(k_0 r) + 2k_0 r\cos(k_0 r))\mathbf{e}_z\mathbf{e}_z\right]$$

$$= \frac{4\pi}{(2\pi k_0 r)^3}\left[(\sin(k_0 r) - k_0 r\cos(k_0 r))\bar{\mathbf{I}} + \left((k_0^2 r^2 - 3)\sin(k_0 r) + 3k_0 r\cos(k_0 r)\right)\mathbf{e}_z\mathbf{e}_z\right]. \tag{50}$$

Due to (48), the Cartesian components $\mathbf{e}_x$, $\mathbf{e}_y$ and $\mathbf{e}_z$ can be replaced by $\hat{\Theta}$, $\hat{\Phi}$ and $\hat{r}$, respectively. Thus, the function can be evaluated in the whole spatial domain. Inserting this expression into (12) together with (39) yields

$$\bar{\mathbf{P}}(\mathbf{r}) = \frac{4\pi}{(k_0 r)^3}\left[\left((k_0^2 r^2 - 1)\sin(k_0 r) + k_0 r\cos(k_0 r)\right)\bar{\mathbf{I}} + \left((3 - k_0^2 r^2)\sin(k_0 r) - 3k_0 r\cos(k_0 r)\right)\hat{r}\hat{r}\right]. \tag{51}$$

Figure 6 shows the PSF using the scenario from (21) and (27). Although some polarimetric distortions are visible in the images, the orientation of the sources can be recognized. The PSF consists of two dyadic parts. The part containing the unit dyad is not causing any polarimetric defects in contrast to the part containing the dyad $\hat{r}\hat{r}$. From

$$\lim_{r\to 0}\bar{\mathbf{P}}(\mathbf{r}) = 4\pi\frac{2}{3}\bar{\mathbf{I}}, \tag{52}$$

it follows that there is no polarimetric error in the center of the PSF for $r \to 0$. Since the amplitude of the PSF decreases with $1/r$, the polarimetric error is localized around the sources.

[†] Note that this is only valid, because the dyad entries are represented using spherical unit vectors.
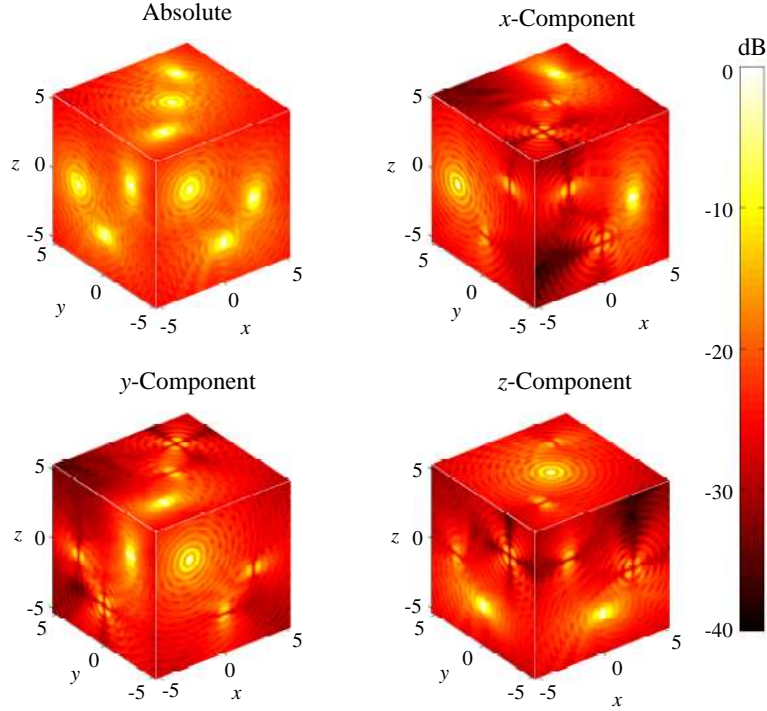
Figure 6. Image of currents positioned as in (21) and oriented as in (27) for a monofrequent spherical k-space acquisition geometry generated using (51) for $\lambda = 1\,\mathrm{m}$ while x, y and z are measured in wavelengths (λ).

3.4. Full Scan Range Finite Bandwidth Approximation

The solution in the last subsection can be extended to finite bandwidth. When it comes to broadband data, however, windowing is very common. For this purpose, the masking function is chosen as

$$M(\mathbf{k}) = W_n(k) = k^{-n} \begin{cases} 1 & k_{\min} \leq k \leq k_{\max} \\ 0 & \text{otherwise} \end{cases}, \tag{53}$$

which incorporates the basic frequency weighting factor k^{-n}. This frequency weighting function has a kind of lowpass characteristic and it allows the PSF to be evaluated analytically.

3.4.1. Scalar

Solving (7) with (53) yields

$$P(\mathbf{r}) = \mathscr{F}\{W_n(k)\} = 4\pi r^{n-3} \Big[h_1(r)\Big]_{k_{\min}}^{k_{\max}}, \tag{54}$$

where

$$h_1(r) = \begin{cases} \sin(kr) - kr\cos(kr), & n = 0 \\ -\cos(kr), & n = 1 \\ \mathrm{Si}(kr), & n = 2 \end{cases} \tag{55}$$

and the sine integral function is defined as

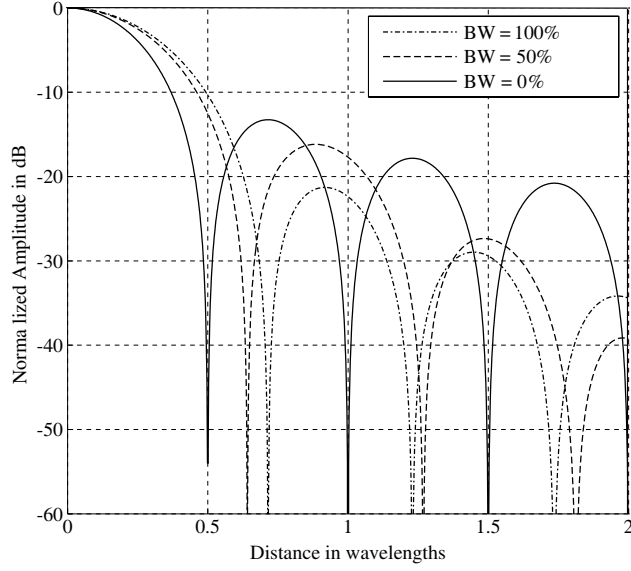$$\mathrm{Si}(x) = \int_0^x \frac{\sin t}{t} dt. \tag{56}$$

Figure 7. Normalized point spread function $\mathscr{F}\{W_0(\mathbf{k})\}$ plotted dependent on the radial distance r in wavelengths $\lambda_{\min}$ for various bandwidths $BW = 1 - \frac{\lambda_{\min}}{\lambda_{\max}}$. $BW = 0\%$ corresponds to Eq. (39).
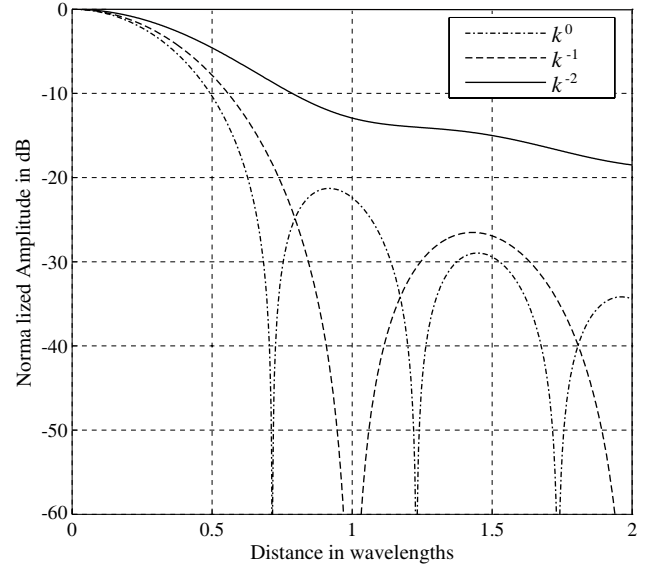
Figure 8. Point spread function $\mathscr{F}\{W_n(\mathbf{k})\}$ plotted dependent on the radial distance r in wavelengths $\lambda_{\min}$ for the frequency window function exponents $n = 0, 1, 2$ while $BW = 1 - \frac{\lambda_{\min}}{\lambda_{\max}} = 100\%$.

The formula for $n = 0$ can also be found in [13, 14] and [15, p. 324]. The result for $n = 2$ can be shown to be identical to the PSF in (37) using

$$ w(k) = \lim_{\Delta k \to 0} \frac{1}{\Delta k} W_2(k) \;\; \text{with} \;\; \begin{aligned} k_{\max} &= k_0 + \Delta k, \\ k_{\min} &= k_0. \end{aligned} \tag{57} $$

The center value of the PSF depends on the bandwidth according to

$$ \lim_{r \to 0} \mathscr{F}\{W_n(k)\} = 4\pi \frac{1}{3-n} \Big[k^{3-n} \Big]_{k_{\min}}^{k_{\max}}. \tag{58} $$

Figure 7 shows how the bandwidth influences the shape of the PSF when the maximum frequency remains constant. Increasing the bandwidth decreases the sidelobes, but it also broadens the main lobe which is bad for the resolution. Fig. 8 illustrates the effect of windowing. As the parameter n increases, the sidelobe level decreases at the cost of a diminishing resolution. In this plot, the complete frequency band down to zero was used. An overview of these phenomena is given in Fig. 9. For comparison, a 3D plot is depicted in Fig. 10.

3.4.2. Dyadic

By applying similar techniques as in the scalar case to the dyadic integral in (12), the second term resolves to

$$ \mathscr{F}\left\{W_n(k)\hat{k}\hat{k}\right\} = \frac{4\pi}{r^3} n^{-\frac{n}{2}} k^{-n} \Big[h_2(r)\bar{\mathbf{I}} + h_3(r)\hat{r}\hat{r} \Big]_{k_{\min}}^{k_{\max}}, \tag{59} $$

where

$$ h_2(r) = \begin{cases} \mathrm{Si}(kr) - \sin(kr), & n = 0 \\ (-\sin(kr)), & n = 1 \\ k^2 r^2 \mathrm{Si}(kr) - \sin(kr) + kr\cos(kr), & n = 2, \end{cases} $$
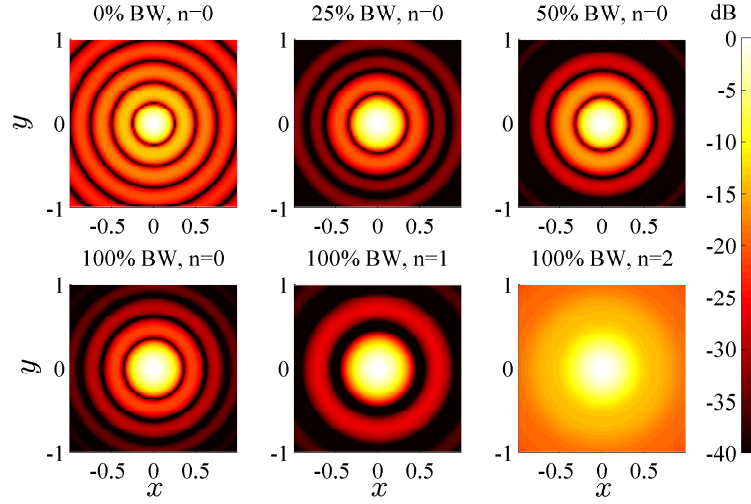
Figure 9. z-cuts of normalized point spread function $\mathscr{F}\{Wn(\mathbf{k})\}$ in (54) plotted in x, y-plane where the unit is scaled by $\lambda_{\min}$ for various frequency window function exponents $n = 0, 1, 2$ and bandwidths, i.e., $BW = 1 - \frac{\lambda_{\min}}{\lambda_{\max}}$.
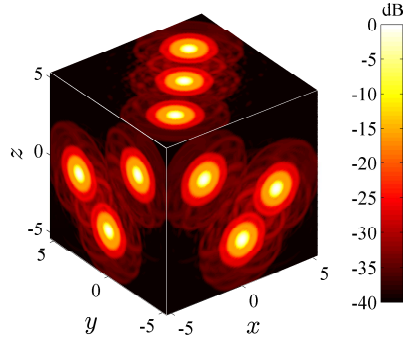

Figure 10. Image of scatterers in (21) for a broadband spherical k-space acquisition geometry generated using (54) for $\lambda_{\max} = 2\,\mathrm{m}$ and $\lambda_{\min} = 1\,\mathrm{m}$ while x, y and z are measured in wavelengths ($\lambda_{\min}$).

$$h_3(r) = \begin{cases} -3\mathrm{Si}(kr) + 4\sin(kr) - kr\cos(kr), & n = 0 \\ 3\sin(kr) - kr\cos(kr), & n = 1 \\ -k^2r^2\mathrm{Si}(kr) + 3\sin(kr) - 3kr\cos(kr), & n = 2. \end{cases}$$

The PSF is obtained by combining this with the scalar result in (55). This leads to

$$\bar{\mathbf{P}}(\mathbf{r}) = \frac{4\pi}{r^3} n^{-\frac{n}{2}} k^{-n} \Big[(h_1(r) - h_2(r))\bar{\mathbf{I}} - h_3(r)\hat{r}\hat{r}\Big]_{k_{\min}}^{k_{\max}} \tag{60}$$

with

$$h_1(r) - h_2(r) = \begin{cases} -\mathrm{Si}(kr) + 2\sin(kr) - kr\cos(kr), & n = 0 \\ \sin(kr) - kr\cos kr, & n = 1 \\ k^2r^2\mathrm{Si}(kr) - kr\cos(kr) + \sin(kr), & n = 2. \end{cases} \tag{61}$$

The center value of the PSF follows from a limit calculation and reads as

$$\lim_{r\to 0} \bar{\mathbf{P}}(\mathbf{r}) = 4\pi \frac{1}{3-n} \frac{2}{3} \bar{\mathbf{I}} \Big[k^{3-n}\Big]_{k_{\min}}^{k_{\max}}. \tag{62}$$
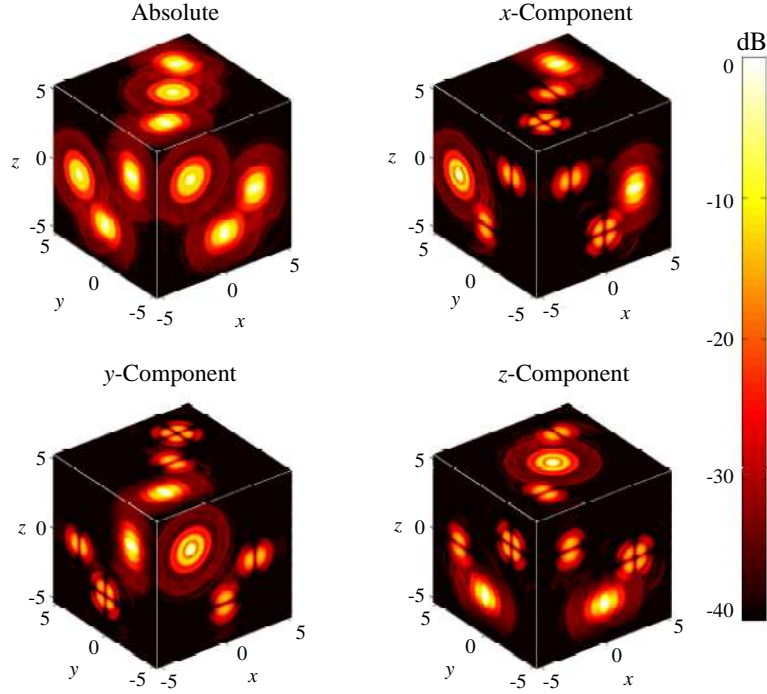
Figure 11. Image of currents positioned as in (21) and oriented as in (27) for a broadband spherical k-space acquisition geometry generated using (60) for $n = 0$, $\lambda_{\max} = 2\,\mathrm{m}$ and $\lambda_{\min} = 1\,\mathrm{m}$ while x, y and z are measured in wavelengths ($\lambda_{\min}$).

Again the polarimetric distortions are vanishing in the center. Fig. 11 shows the PSF for $n = 0$ using the well-known scenario from (21) and (27). In contrast to Fig. 6, the dynamic range has been increased drastically.

4. NUMERICAL VERIFICATION

In this section, the analytical PSFs derived in the previous section are verified using a numerical implementation of the imaging procedure in the k-space domain. The k-space is sampled using a Gauss-Legendre sampling grid for the angular sampling and an equidistant sampling grid in the radial direction. The sampling resolution depends on the electrical size of the imaging region. Details for the appropriate implementation of the imaging algorithm can be found in [13].

Since scalar PSFs are related to dyadic PSFs, it is sufficient to verify the results obtained with the latter ones. The dyadic PSF in Section 3.3 was already verified via (57). Therefore, it remains to investigate the accuracy of the PSFs in Section 3.1 and Section 3.2 based on narrow angle approximations and of the dyadic PSF in Section 3.4.

4.1. Narrow Angular Scan Range

To verify the PSFs in (24) and (32) based on a narrow angle approximation, the scenario described in (21) is used. The k-space acquisition domain is described by

$$|\theta - \pi/2| \leq \pi/256, \quad |\phi - \pi/6| \leq \pi/128, \quad \frac{\lambda}{1\,\mathrm{m}} \in [1.0; 2.0]. \tag{63}$$

The full vectorial currents in the image are evaluated on the line

$$\frac{x}{\lambda_{\min}} = -3, \ldots, 3, \quad \frac{y}{\lambda_{\min}} = 2, \quad \frac{z}{\lambda_{\min}} = 2. \tag{64}$$
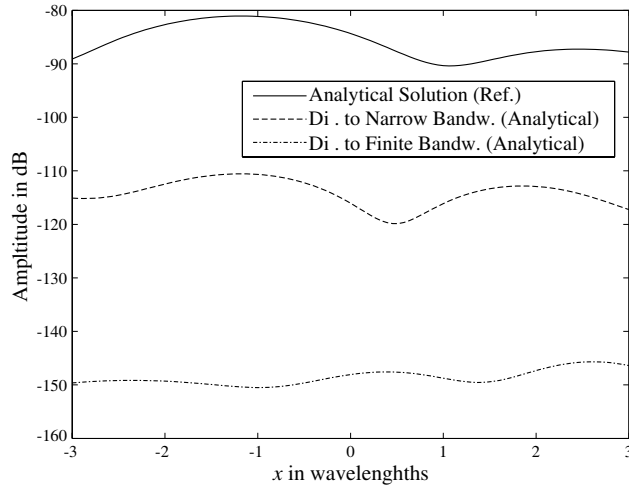
Figure 12. Comparison of images generated numerically and by PSFs in (24) and (32) using the currents described in (21) and evaluated on the line described by (64) with the parameters in (63).
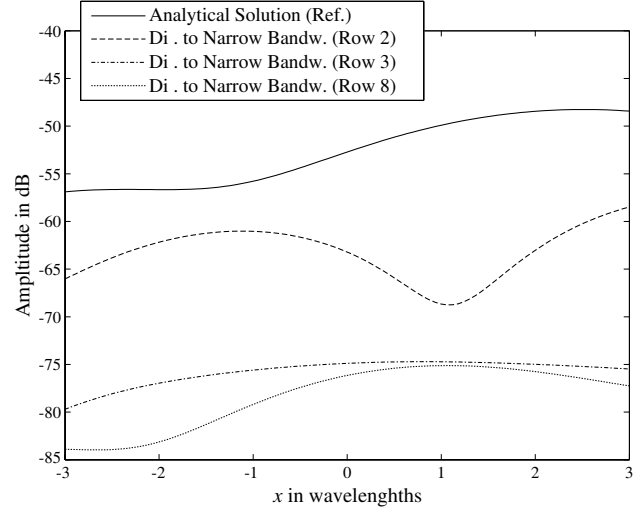
Figure 13. Comparison of images generated numerically and by PSFs in Table 2 using the currents described in (21) and evaluated on the line described by (64) with the parameters in (65).

Since the dyadic PSFs in (24) and (32) employ an approximation which is only accurate for very small aspect angles, it is inadequate to use the PSFs to compute a reference solution. Instead, a very accurate numerical solution is used as a reference. The high accuracy is achieved by using a k-space oversampling factor of 10. This solution is depicted in Fig. 12 by the solid line. The two other lines are error levels indicating the complex vectorial difference to the solid reference solution. The dashed line corresponds to the error level of the PSF in (24). As can be seen, the accuracy seems to be reasonably good. Since numerical and analytical techniques have been combined here, this is referred to as mixed solution in the plot. The third curve depicts the error level of the PSF in (32). The remaining error level is identified as an implication of the narrow angle approximations of the PSFs.

In this paragraph, the performance of the PSFs in Table 2 shall be analyzed. The angular scan range is increased and the bandwidth is reduced as given by

$$|\theta - \pi/2| \leq \pi/5, \quad |\phi - \pi/6| \leq \pi/4, \quad \frac{\lambda}{1\,\mathrm{m}} \in [1.0; 1.1]. \tag{65}$$

Figure 13 depicts the error curves for the PSFs corresponding to the rows 2, 3 and 8 of Table 2. Obviously, a more sophisticated approximation reduces the error. The parameter set from the third row of the table produces already quite good results. This implies that the expansion order of the exponent seems to be more important than the expansion order of the prefactor.

4.2. Full Scan Range

For the verification of the PSF in Section 3.4, it makes sense to use the analytical solution as a reference, because no approximations could possibly corrupt the reference solution in this case. The source configuration and observation line remains unchanged. The k-space acquisition domain is defined in (63). The solid curve in Fig. 14 corresponds to the analytical reference solution in (60). The two other curves are error curves which show the absolute value of the complex difference between the numerical solutions and the reference. The individual lines were obtained by setting the oversampling factor to 2 and 4, respectively. By increasing the oversampling factor and thus the accuracy of the numerical algorithm, the error decreases. So the analytical PSF is able to predict the images very accurately.
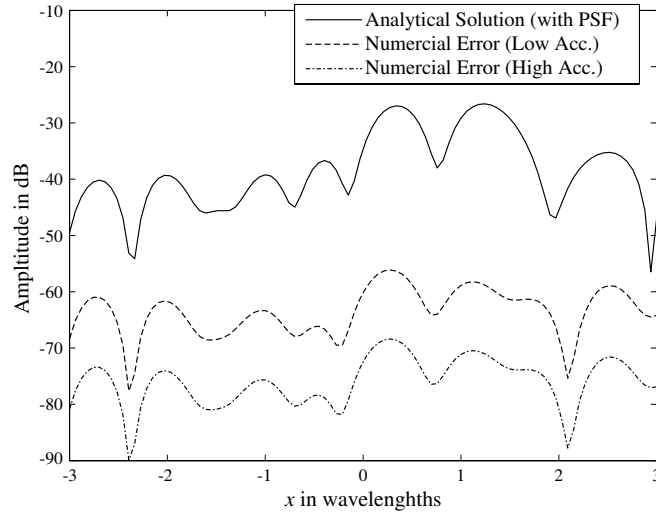
Figure 14. Comparison of images generated numerically and by PSFs in (60) using the currents described in (21) and evaluated on the line described by (64).

5. CONCLUSION

In the beginning of this work, two imaging scenarios were presented, where the imaging process has been described by the convolution with a so-called point spread function (PSF). In these scenarios, computing the PSF means to calculate a 3D Fourier integral. This can be done analytically in some cases. In this work, a collection of new formulas was derived with the assistance of a computer algebra system. A numerical imaging algorithm was employed to verify the formulas. The results in this work are expected to be useful for the simulation of broadband vectorial imaging systems and for the fast generation of images by ray based algorithms.

REFERENCES

1. Sarty, G. E., R. Bennet, and R. W. Cox, "Direct reconstruction of non-Cartesian k-space data using a nonuniform fast Fourier transform," *Magnetic Resonance in Medicine*, Vol. 45, 908–915, 2001.

2. Basu, S. and Y. Bresler, "An $O(N^2 \log_2 N)$ filtered back-projection reconstruction algorithm for tomography," *IEEE Trans. on Image Process.*, Vol. 9, No. 10, 1760–1773, Oct. 2000.

3. Boag, A., "A fast multilevel domain decomposition algorithm for radar imaging," *IEEE Trans. on Antennas and Propag.*, Vol. 49, No. 4, 666–671, Apr. 2001.

4. Schnattinger, G., C. Schmidt, and T. Eibert, "3-D imaging by hierarchical disaggregation," *German Microwave Conference (GeMiC)*, 1–4, Mar. 2011.

5. Desai, M. D. and W. K. Jenkins, "Convolution backprojection image reconstruction for spotlight mode synthetic aperture radar," *IEEE Trans. on Image Process.*, Vol. 4, No. 4, 505–517, 1992.

6. Mensa, D. L., *High Resolution Radar Cross-section Imaging*, Revised edition, Artech House Inc., 1990.

7. Majumder, U. K., M. A. Temple, M. J. Minardi, and E. G. Zelnio, "Point spread function characterization of a radially displaced scatterer using circular synthetic aperture radar," *IEEE Radar Conference*, 729–733, Apr. 2007.

8. Maussang, F., F. Daout, G. Ginolhac, and F. Schmitt, "GPS ISAR passive system characterization using point spread function," *New Trends for Environmental Monitoring Using Passive Systems*, 1–4, Oct. 2008.

9. Tathee, S., Z. J. Koles, and T. R. Overton, "Image restoration in computed tomography: Estimation of the spatially variant point spread function," *IEEE Trans. on Med. Imag.*, Vol. 11, No. 4, 539–545, Dec. 1992.

10. Gallatin, G. M., "Analytic evaluation of the intensity point spread function," *Journal of Vaccum Science and Technology B*, Vol. 18, No. 6, 3023–3028, Nov. 2000.

11. Berizzi, F., E. Mese, M. Diani, and M. Martorella, "High-resolution ISAR imaging of maneuvering targets by means of the range instantaneous Doppler technique: Modeling and performance analysis," *IEEE Trans. on Image Process.*, Vol. 10, No. 12, 1880–1890, Dec. 2001.

12. Buddendick, H. and T. F. Eibert, "Bistatic image formation from shooting and bouncing rays simulated current distributions," *Progress In Electromagnetics Research*, Vol. 119, 1–18, 2011.

13. Schnattinger, G. and T. F. Eibert, "Solution to the full vectorial 3D inverse source problem by multi-level fast multipole method inspired hierarchical disaggregation," *IEEE Trans. on Antennas and Propag.*, Vol. 60, No. 7, 3325–3335, Jul. 2012.

14. Schnattinger, G., C. H. Schmidt, and T. F. Eibert, "Analysis of 3-D images generated by hierarchical disaggregation," *Proc. Int. Radar Symp. (IRS)*, 365–370, Leipzig, Germany, Sep. 2011.

15. Råde, L. and B. Westergren, *Mathematics Handbook for Science and Engineering*, 5th edition, Springer, 2004.

16. Rosenthal, A., D. Razansky, and V. Ntziachristos, "Fast semi-analytical model-based acoustic inversion for quantitative optoacoustic tomography," *IEEE Trans. on Image Process.*, Vol. 29, No. 6, 1275–1285, 2010.

17. Balanis, C., *Advanced Engineering Electromagnetics*, ser. CourseSmart Series, Wiley, 2012, [Online]. Available: http://books.google.de/books?id=cRkTuQAACAAJ.

18. Stratton, J. A., *Electromagnetic Theory*, M. E. El-Hawary (ed.), IEEE Press, 2007.

19. Woods, J. W., *Multidimensional Signal, Image, and Video Processing and Coding*, Academic Press, 2011.

20. SciFace Software, *MuPAD* (Multi Processing Algebra Data Tool), SciFace Software, Paderborn, Germany, 2012, www.mupad.de.

21. The MathWorks Inc., *MATLAB* (Matrix Laboratory), The MathWorks Inc., Natick, Massachusetts, USA, 2012, www.mathworks.com.